https://doi.org/10.5194/wes-2026-144
Preprint. Discussion started: 10 September 2026

eawe european academy of wind energy
Open Access WIND ENERGY SCIENCE DISCUSSIONS

Fleet-scale evidence and a testable coupled mechanism for radial-raceway spalling in an offshore 5 MW three-row roller main bearing

Xilei Ma[1,2], Dongxiang Jiang[2], Kai Zhang[1]

1 CSSC Science & Technology Co., Ltd., Shanghai 200023, China; 2 Department of Energy and Power Engineering, Tsinghua University, Beijing 100084, China

Correspondence to: Xilei Ma (mxl22@mails.tsinghua.edu.cn)

Abstract. Standard rating-life calculations predicted sufficient durability, yet premature radial outer-raceway spalling recurred in a 203-turbine offshore 5/6.2 MW fleet. By 11 August 2026, eight bearings had been removed after 26–53 months and two additional units were stopped awaiting replacement. All eight dismantled bearings exhibited damage within the stationary 3–9 o'clock lower radial load zone, whereas axial-row damage was limited. Fleet-scale teardown evidence for offshore three-row cylindrical-roller main bearings is rarely reported in the peer-reviewed wind-energy literature. The present dataset therefore provides an unusual opportunity to establish a repeatable circumferential damage pattern and to organize competing mechanisms within an explicit evidence hierarchy. Roller-end breakage, gearbox-side cage contact, a measured full-power inner-to-outer-ring temperature difference of about 12 °C, and partly obstructed grease inlets provide mutually consistent, but individually non-unique, evidence for load redistribution and lubrication-access effects. Grease screening of 198 turbines identified Cu ≥ 5000 ppm in 21 units (10.61%), Fe ≥ 5000 ppm in 10 units (5.05%), and the combined condition Cu > 10000 ppm and Fe > 5000 ppm in five units (2.53%); these thresholds are used only as project-specific risk flags, not as transferable diagnostic cut-offs. A nominal Hertz calculation gives a baseline maximum roller load of about 109 kN and contact pressure of 0.997 GPa. System FEA predicts 0.067° maximum raceway misalignment; across the 100 mm roller length this corresponds to an end-to-end geometric offset of about 0.12 mm, providing an order-of-magnitude structural basis for testing a moderate 20–50% edge-pressure amplification range (Kedge = 1.20–1.50), while not constituting a calibration of Kedge. The combined evidence is most consistent with accelerated rolling contact fatigue in which the fixed load zone controls damage location, while thermo-structural load redistribution, restricted grease replenishment, debris and local case-condition variability can reduce fatigue margin. The principal contribution is therefore fleet-scale field evidence and an evidence-ranked, falsifiable engineering framework for offshore main-bearing failure assessment, rather than identification of a unique root cause or a new life-prediction equation.

Keywords. rolling contact fatigue; wind turbine main bearing; three-row roller bearing; operating clearance; grease delivery; edge loading.

1 Introduction

The main bearing of a large offshore wind turbine carries rotor gravity, aerodynamic thrust, overturning moment, yaw-error loads and transient impact loads. It is therefore a critical structural-integrity component in the drivetrain. Compared with conventional industrial bearings, wind-turbine main bearings operate at low speed, high load, large diameter, variable loading and grease lubrication, with limited maintenance access. Their failure can cause expensive crane operations, bearing replacement and extended power-production losses. Identifying the premature-failure mechanism from a fatigue and fracture mechanics perspective is therefore important for offshore wind reliability (IEC, 2019; Kenworthy et al., 2024; Hart et al., 2020; Harris and Kotzalas, 2006; Johnson, 1985).

This paper addresses a scientific inference problem rather than a single-component root-cause claim: which mechanisms are required to explain the repeated spatial morphology of premature radial-raceway spalling, and which observations merely modify their plausibility? The emphasis is intentionally placed on fleet-scale field evidence and engineering inference rather than on claiming a new microscopic failure mechanism. Public main-bearing literature has established the importance of structural deformation, lubrication, load distribution, damage detection and rating-life uncertainty, but fleet-scale teardown evidence for large offshore three-row cylindrical-roller main bearings remains scarce (Hart et al., 2020; Kenworthy et al., 2024; Quick et al., 2026; Kestel et al., 2026). The aim is therefore to combine recurrence across a 203-turbine population, eight dismantled bearings, field inspections and transparent mechanics-based sensitivity calculations while preserving the distinction between observation, model-supported plausibility and unmeasured causality.

Premature wind-turbine bearing failure may involve rolling contact fatigue, micropitting, abrasive wear, boundary lubrication, false brinelling, white etching cracks (WECs), white etching areas (WEAs) and insufficient heat-treatment fatigue margin (Harris and Kotzalas, 2006; Johnson, 1985; Hamrock and Dowson, 1981; Sadeghi et al., 2009; Lee et al., 2025; Ren et al., 2025; Chen et al., 2024; Kawiak and Sajek, 2025; Yin et al., 2024; Lopez-Urunuela et al., 2021; Spille et al., 2021; Mayweg et al., 2021). ISO 281 and ISO/TS 16281 are appropriate engineering bases for rating life and load sensitivity, but the field-life gap remains an active scientific issue because load distribution and rating life depend on model fidelity, structural elasticity, operating conditions and lubrication assumptions (ISO, 2007; ISO, 2008; Hart et al., 2020; Kenworthy et al., 2024; Quick et al., 2026). For grease-lubricated main bearings, simplified elastohydrodynamic formulas also require careful interpretation because starvation, non-steady operation and grease rheology are not represented by a steady fully flooded oil-film calculation (Hart et al., 2022a, b).

The study concerns a three-row cylindrical roller single main bearing used on an offshore 5 MW turbine and fielded across a related 5/6.2 MW fleet. Eight dismantled bearings showed severe radial outer-raceway damage in stationary lower-load-zone sectors spanning 3-9 o'clock, with comparatively less axial-row damage. One roller exhibited severe spalling and edge breakage; cage wear and gearbox-side contact recurred. Grease screens showed elevated Fe and Cu in subsets of the fleet, and selected outer-ring samples showed non-uniform radial case condition. These observations motivate a coupled local-contact fatigue analysis, but no single observation is treated as sole causal proof.

https://doi.org/10.5194/wes-2026-144
Preprint. Discussion started: 10 September 2026

The central innovation is the field evidence structure. Such fleet-scale teardown evidence for offshore three-row cylindrical-roller main bearings is rarely reported in peer-reviewed wind-energy literature. In the present 203-turbine offshore fleet, multiple dismantled bearings show a repeated 3–9 o'clock spatial distribution of radial-raceway spalling, allowing that recurrent field pattern to be connected to an explicit evidence-ranked coupled-failure framework. First, common morphology is mapped against fleet exposure and the stationary radial load zone. Second, measured ring-temperature differences and lubrication-path inspection are combined with rating calculations, Bladed loads, system FEA and contact-mechanics sensitivity analysis. Third, the case-depth-to-shear-depth ratio SHD/z_tau is used only as a descriptive screening ratio, with no acceptance threshold or claim of validated fatigue-life prediction. Fourth, direct observations, mechanics-based inferences and testable hypotheses are separated explicitly so that engineering decisions can be made without converting plausible mechanisms into asserted root causes. The intended scientific advance is therefore a reproducible way to organize heterogeneous field evidence around a recurrent failure morphology, rather than deeper microscopic mechanism resolution than dedicated tribology or failure-analysis studies.

2 Study object, methods, and data sources

2.1 Main bearing structural parameters

The turbine has a rated power of 5 MW, a rotor diameter of 151 m and a rated full-power wind speed of approximately 11 m/s. Based on the bearing calculation report and local control-parameter reconciliation, the full-power/rated platform rotor speed is taken as 10.1 r/min for the following load and contact calculations.

Table 1: Main bearing structural and operating parameters.

Parameter	Value
Bearing drawing number	Withheld for commercial confidentiality reasons
Bearing mass	18,200 kg
Outer diameter	3206 mm
Main bore diameter	1964 mm
Pitch radius	1292.5 mm
Pitch diameter	2585.0 mm
Number of radial rollers	72
Radial roller size	diameter 89.95 mm x 100 mm
Number of axial rollers	2 x 180
Axial roller size	diameter 80.00 mm x 80 mm; diameter 79.95 mm x 80 mm
Radial clearance	0.45-0.55 mm
Grease	Mobil SHC Grease 460 WT
Grease quantity	55.7 kg, about 60% filling

https://doi.org/10.5194/wes-2026-144
Preprint. Discussion started: 10 September 2026

WIND ENERGY SCIENCE DISCUSSIONS

Parameter	Value
Circumferential grease inlets	8, M22 x 1.5-30 deep
Grease outlets	8, diameter 40 mm

2.2 Fleet exposure and grease-screening database

The fleet comprised 203 turbines. By 11 August 2026, eight bearings had been removed (8/203, 3.94%) and two additional units were stopped awaiting replacement, giving 10/203 (4.93%) turbines classified as affected at the study cut-off. These are descriptive cumulative affected fractions at one calendar cut-off, not estimates of lifetime failure probability. A time-to-event analysis was not performed because turbine-specific commissioning dates, exposure histories, right-censoring times and the selection process leading to bearing removal were not available in a harmonized form. The eight removed bearings had operated for 26–53 months (median 48 months), but this range is descriptive only and cannot be used to construct a Kaplan–Meier curve, hazard function or incidence rate. Grease records were screened for 198 units (198/203, 97.54%). Cu and Fe concentrations are reported in ppm in the source records: 21 units (10.61%) had Cu $\geq$ 5000 ppm, 14 (7.07%) had Cu > 10000 ppm, 10 (5.05%) had Fe $\geq$ 5000 ppm, three (1.52%) had Fe > 10000 ppm, and five (2.53%) simultaneously had Cu > 10000 ppm and Fe > 5000 ppm. These thresholds were defined within the project for screening and are not presented as transferable diagnostic cut-offs. Because grease age, sampling position, sampling interval and reporting conditions were not harmonized across all records, the concentration data are used for risk stratification rather than causal or prognostic inference.

2.3 Common macroscopic failure morphology

Eight removed bearings were disassembled and compared. All exhibited radial outer-raceway damage in the fixed lower load zone, although the circumferential extent varied by unit:

https://doi.org/10.5194/wes-2026-144
Preprint. Discussion started: 10 September 2026

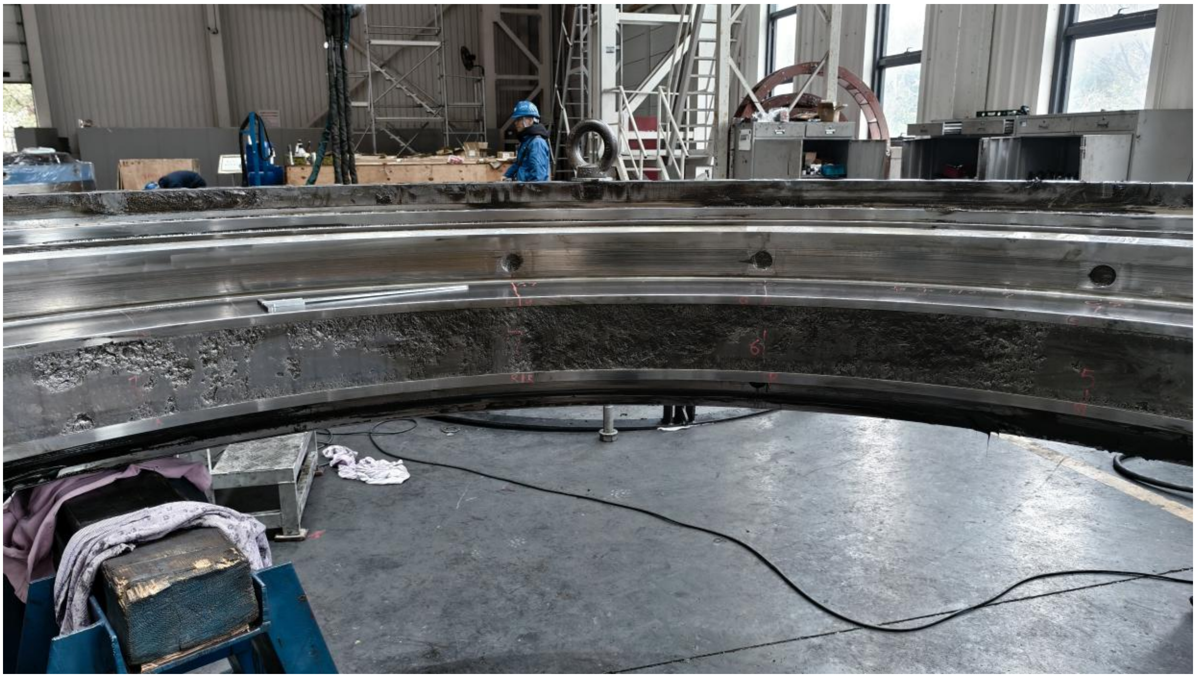

Figure 1: Field photograph of continuous belt-like spalling on the radial outer raceway of a representative dismantled bearing. The image has been re-encoded without report overlays; diagnostic surface features have not been digitally altered.

Across the fleet, damaged sectors lay within the lower half between 3 and 9 o'clock; individual units included 3-9, 4-7, 5-7 and 5-9 o'clock extents. The illustrated sample had maximum loss near 5-7 o'clock.

https://doi.org/10.5194/wes-2026-144
Preprint. Discussion started: 10 September 2026

Open Access
WIND ENERGY SCIENCE
DISCUSSIONS

Figure 2: Field photographs of (a) representative roller-end spalling and (b) copper-alloy cage wear observed during teardown. The photographs have been recomposed without internal report labels.

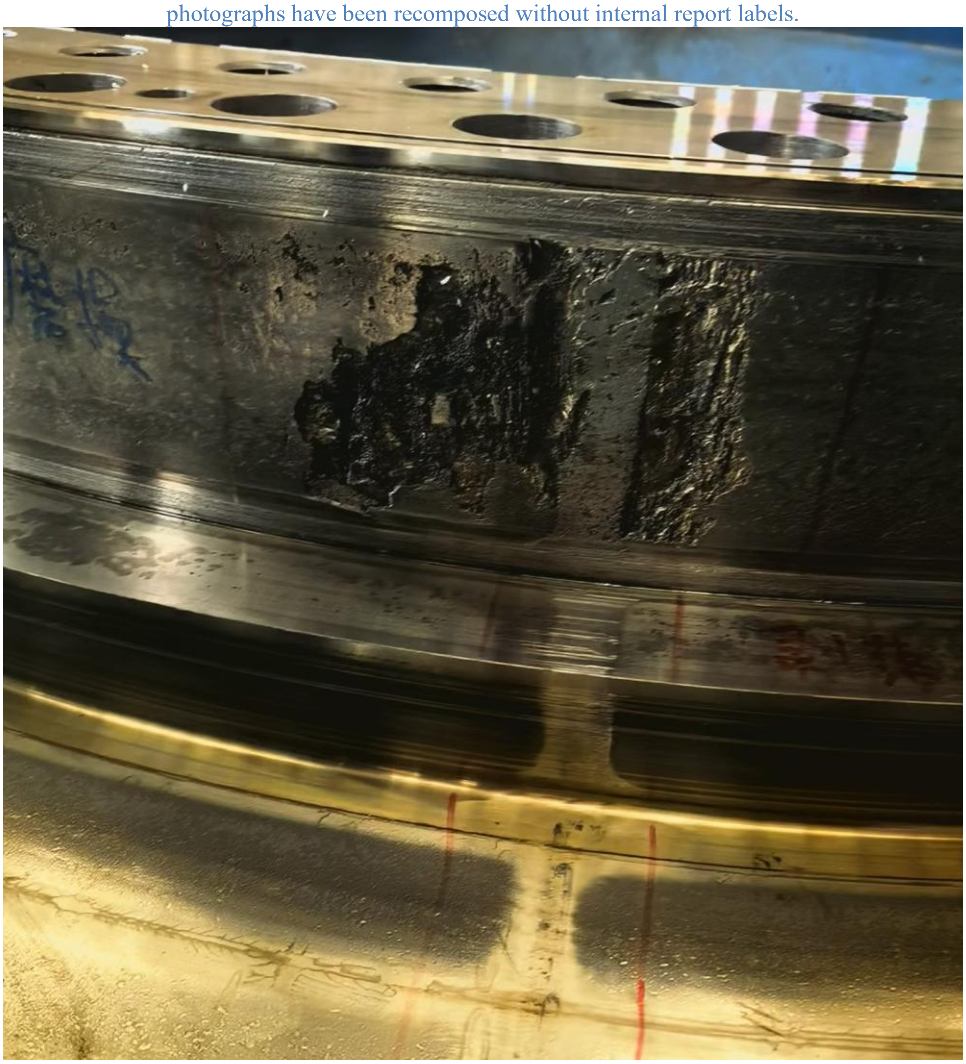

Figure 3: Field photograph comparing severe radial outer-raceway spalling with comparatively intact adjacent raceway regions. The image has been re-encoded without report overlays.

2.4 Material tests: metallography, hardness, and case depth

Third-party tests for selected OR_A and OR_B outer-ring samples are summarized in Table A2. On OR_B, unworn 12-o'clock radial sections had effective case depths of 4.87-5.03 mm compared with 6.07-6.29 mm on axial raceways. OR_A loaded-zone radial sections showed 1.49 mm effective case depth or severely reduced residual hardness after damage. Because loaded-zone samples were worn or spalled, they cannot reconstruct the original manufactured state by themselves. The material data therefore demonstrate non-uniform remaining case condition and reduced local fatigue margin; a manufacturing-conformity conclusion requires drawing acceptance limits and unworn multi-circumferential sections.

https://doi.org/10.5194/wes-2026-144
Preprint. Discussion started: 10 September 2026

2.5 Thermal-clearance and lubrication-path evidence

During full-power operation, the available measurement showed the inner-ring temperature about 12 °C above the outer ring at the 6 o'clock position. The shaft segment between the gearbox and bearing was about 15 °C colder than the inner ring; therefore, this observation does not support gearbox heat transfer as the primary heat source at that time. Differential ring expansion provides a physically plausible pathway for reducing operating radial clearance, but the present temperature observation is not a fleet distribution and cannot quantify hot clearance without a coupled thermal-clearance model.
The system design specifies 40 L/year total grease addition, including 20 L/year for the radial row. Teardown showed the radial cage displaced toward the gearbox side, with local wear and geometry capable of partly obscuring a gearbox-side inlet. Outlet discharge was also non-uniform. These observations support a grease-path restriction hypothesis while leaving actual contact-inlet flow unmeasured.

2.6 Rating calculations, system simulation, and grease-monitoring data

To avoid single-sample attribution, the study combines bearing rating calculations, system finite-element simulation and operating grease screens. The rating calculation for the studied bearing follows ISO 281 and ISO/TS 16281 and uses Mobil SHC Grease 460 WT (ISO, 2007; ISO, 2008). The author-supplied system finite-element analysis checks bolt load, raceway displacement, mounting-surface tilt, raceway misalignment and mounting-surface contact under a static extreme load. These system-level outputs are used to identify plausible deformation pathways, not to infer roller-resolved field contact pressure. Published work similarly shows that main-bearing load distribution and rating life are sensitive to drivetrain/housing elasticity and model fidelity (Ishihara et al., 2025; Quick et al., 2026). Grease results are used for risk stratification only because particle morphology and contact-inlet flow were not measured across the fleet.

2.7 Bladed extreme-load simulation data

To strengthen the drivetrain-load basis, the analysis uses author-supplied Bladed extreme-load datasets for LM61.5–LM73.5 blades, including load outputs in the rotating hub-centre, tower-top and blade-root coordinate systems. For main-bearing rolling contact fatigue, the rotating hub-centre loads are most directly relevant. Fx is treated as the axial load along the main-shaft direction, Fyz as the radial resultant perpendicular to the shaft, Mx as main-shaft torque and Myz as the bending-moment resultant carried by the main bearing. Because the studied rotor diameter is 151 m, LM73.5 loads are used as the main basis.
Across the LM73.5 design-extreme dataset, the maximum radial resultant Fyz reaches 1.9346 MN and the maximum bending resultant Myz reaches 22.019 MN m; importantly, these maxima occur in different load cases and are not combined here as a simultaneous field load state. The dataset therefore demonstrates the relevance of both radial loading and large bending moments, but it does not reconstruct the load history of any failed turbine. Mounting-surface tilt and roller edge loading must be interpreted together with this distinction. This use of design-extreme data is consistent with published three-dimensional

https://doi.org/10.5194/wes-2026-144
Preprint. Discussion started: 10 September 2026

drivetrain and local-raceway analyses, while remaining separate from event-specific failure reconstruction (Ishihara et al., 2025; Wang et al., 2022).

2.8 Independent failure analyses and severe-damage grease reports

The supplementary evidence includes independent inspections and grease tests of damaged units. One same-type severe-failure sample outside the primary eight-bearing teardown case series showed WEC microstructures near propagating cracks and spalling pits, whereas the OR_A/OR_B reports did not identify WEC/WEA. Because that WEC-positive sample is not part of the primary fleet teardown set, it is used only as contextual evidence that WEC can occur in this bearing type and is excluded from claims about the prevalence or initiation mechanism in the eight dismantled bearings. Project 2 also showed clearance increase associated with extensive raceway/cage abrasion, and five severe-damage grease datasets contained steel and copper wear particles. These observations support possible abrasive-wear and crack-growth pathways but do not establish WEC/WEA or grease chemistry as a universal initiating cause.

2.9 Evidence hierarchy and inference boundaries

Evidence is classified before mechanism interpretation in order to prevent model assumptions from being presented as field measurements. Three classes are used. Class D (direct observation) contains quantities or morphology recorded from the fleet, teardown, measurement or third-party test without requiring the proposed mechanism to be true. Class I (mechanics-based inference) contains consequences obtained by applying an explicit model to observed or documented inputs; these results can establish plausibility and sensitivity but do not calibrate an unmeasured field quantity. Class H (testable hypothesis) contains causal links that remain unmeasured and are stated in falsifiable form. A mechanism is described as 'supported' only when more than one Class-D observation is mutually consistent with a Class-I prediction and no direct observation contradicts it. Terms such as 'caused', 'demonstrates the root cause' or 'proves' are avoided for Class-I and Class-H statements. This classification is applied throughout Sects. 4 and 5 and is summarized in Table 2.

Table 2: Evidence classification used for causal statements in this study.

Class	Definition	Examples in this study	What it can support	Language permitted
D: direct observation	Recorded without assuming the proposed mechanism	3–9 o'clock damage sectors; roller-end damage; cage/inlet geometry; temperatures; material tests; fleet counts	Existence, location, measured state or repeated association	observed; measured; recorded; showed
I:mechanics-based inference	Result of an explicit model applied to documented inputs and stated assumptions	Nominal Hertz stress; radial-load sensitivity; Kedge pressure sweep; idealized film-ratio sensitivity	Physical plausibility, direction and order-of-magnitude sensitivity	consistent with; supports plausibility; would increase/decrease if

https://doi.org/10.5194/wes-2026-144
Preprint. Discussion started: 10 September 2026

eawe european academy of wind energy
Open Access WIND ENERGY SCIENCE DISCUSSIONS

Class	Definition	Examples in this study	What it can support	Language permitted
H: testable hypothesis	Causal link not directly measured and capable of being confirmed or rejected by new data	Hot-clearance reduction; restricted contact-inlet flow; roller-end stress concentration; local initiation pathway	Prospective mechanism to be tested	may; could; hypothesis; predicts that

3 Analytical framework and model inputs

3.1 Rated-state load scales and a non-standard comparison index

170 The rotor radius is R = 75.5 m, the rated full-power rotor speed is n = 10.1 r/min, and the rated wind speed is Vw = 11 m/s. The swept area is:

$$A = \pi R^2 = \pi \times 75.5^2 = 1.791 \times 10^4 \text{ m}^2 \tag{1}$$

$$\omega = \frac{2\pi n}{60} = \frac{2\pi \times 10.1}{60} = 1.058\text{rad/s} \tag{2}$$

$$v_{\text{tip}} = \omega R = 1.058 \times 75.5 = 79.9 \text{ m/s} \tag{3}$$

$$\lambda_{\text{tip}} = \frac{v_{\text{tip}}}{V_w} = \frac{79.9}{11} = 7.26 \tag{4}$$

At the rated power Pr = 5.0 MW, the main drivetrain torque is:

175
$$T = \frac{P_r}{\omega} = \frac{5.0 \times 10^6}{1.058} = 4.73 \times 10^6\text{Nm} = 4.73\text{MNm} \tag{5}$$

With air density ρ = 1.225 kg/m^3 and a thrust coefficient of 0.45, the aerodynamic thrust at rated wind speed is:

$$F_T = \frac{1}{2}\rho A C_T V_w^2 = \frac{1}{2} \times 1.225 \times 1.791 \times 10^4 \times 0.45 \times 11^2 = 5.97 \times 10^5 \text{ N} = 0.60\text{MN} \tag{6}$$

Using an equivalent thrust lever arm of 8 m, the thrust-induced overturning moment is:

$$M_T = F_T L_T = 0.597 \times 8 = 4.78\text{MNm} \tag{7}$$

180 For descriptive scaling only, the source engineering calculation combined axial force, radial force and a moment-equivalent force into the following non-standard comparison index:

$$P_{\text{eq}} = XF_r + YF_a + \frac{M_T}{d_m} \tag{8}$$

Retaining the coefficients used in that engineering screen (X = 1.0 and Y = 0.67), together with radial load 1.50 MN, axial load 0.597 MN and mean diameter 2.585 m, gives:

https://doi.org/10.5194/wes-2026-144
Preprint. Discussion started: 10 September 2026

$$P_{\mathrm{eq}} = 1.0 \times 1.50 + 0.67 \times 0.60 + \frac{4.78}{2.585} = 3.75\mathrm{MN} \tag{9}$$

This quantity is not an ISO/TS 16281 equivalent dynamic bearing load and is not used in the subsequent Hertzian stress, film-ratio or rating-life calculations. It is retained only to show the relative force scale of rated thrust, radial load and the moment-equivalent term; bearing internal load distribution is taken from the separate rating/system analyses.

3.2 Circumferential load distribution of radial rollers

For angular loads on radial rollers, the Stribeck load distribution is adopted:

$$Q_j = Q_{\max}\left[1 - \frac{1}{2\varepsilon}\left(1 - \cos\psi_j\right)\right]^t \tag{10}$$

where Q_j denotes the normal load acting on the j-th roller, $Q_{\max}$ is the maximum roller load within the loaded zone, ψ_j represents the angular position of the j-th roller relative to the load center at the 6 o'clock position, ε is the load distribution parameter, and t stands for the load-deflection exponent. For line-contact cylindrical rollers, the exponent is taken as:

$$t = \frac{10}{9} \tag{11}$$

Field damage occupied a broad lower-half envelope from 3 to 9 o'clock, i.e. approximately 180° around the stationary outer ring. That envelope is a cumulative damage map and is not assumed to equal the instantaneous Hertzian load-support angle. For the compact Stribeck calculation, the core analytical load zone is idealized as 4–8 o'clock, centered at 6 o'clock, corresponding to +/-60° (120° total). With 72 radial rollers, the circumferential pitch is 5°. The discrete sector from -60° to +60° therefore contains 25 roller-centre positions (24 pitch intervals); the two boundary positions carry zero load by Eq. (13), leaving 23 positive-load positions in the idealized model. The 4–8 o'clock sector is thus a symmetric core-load representation nested inside the observed 3–9 o'clock damage envelope, not a fitted boundary of field damage.

$$\psi_0 = 60° \tag{12}$$

The roller load equals zero at the boundary of the loaded zone, which yields the constraint:

$$1 - \frac{1}{2}\varepsilon(1 - \cos\psi_0) = 0 \tag{13}$$

Substituting $\psi_0 = 60°$ into Eq. (13) gives:

$$\varepsilon = \frac{1 - \cos 60°}{2} = 0.25 \tag{14}$$

https://doi.org/10.5194/wes-2026-144
Preprint. Discussion started: 10 September 2026

The total number of radial rollers is $Z_r = 72$, corresponding to an angular pitch of:

$$\Delta\psi = \frac{360^\circ}{Z_r} = \frac{360^\circ}{72} = 5^\circ \tag{15}$$

The radial load equilibrium condition is expressed as:

$$\sum_{j=1}^{Z_r} Q_j \cos\psi_j = F_r \tag{16}$$

Substitute Eq. (10) into Eq. (16) to obtain the maximum load on a single roller:

$$Q_{\max} = \frac{F_r}{\sum_{j=1}^{Z_r}\left[1 - \frac{1}{2\varepsilon}(1 - \cos\psi_j)\right]^t \cos\psi_j} \tag{17}$$

Equation (17) is evaluated directly rather than introducing an empirical roller-count or load-distribution multiplier. Using epsilon = 0.25, t = 10/9 and roller-centre angles from -60° to +60° at 5° increments, the dimensionless equilibrium denominator sum{[1 - (1/(2 epsilon))(1 - cos psi_j)]^t cos psi_j} is 13.700. For Fr = 1.50 MN, Eq. (17) therefore gives Qmax = 1.50 MN / 13.700 = 109.5 kN. This value is fully determined by the stated idealized Stribeck assumptions; it is still a nominal screening load because hot clearance, ring/support flexibility, roller crowning and three-dimensional internal load sharing are not resolved.

$$Q_{\max} = 1.09 \times 10^5\ \mathrm{N} = 109\mathrm{kN} \tag{18}$$

3.3 Hertzian line contact and subsurface shear stress

Roller–raceway contact is estimated using classical Hertzian line-contact theory (Johnson, 1985). This analytical Hertz model cannot replace full 3D finite-element contact simulation for accurate stress characterization, but it provides the load-to-stress conversion needed to discuss rolling contact fatigue (Sadeghi et al., 2009; Ren et al., 2025; Chen et al., 2024).

The diameter of radial rollers is 89.95 mm, yielding the roller radius as:

$$R_1 = \frac{89.95}{2} = 44.975\ \mathrm{mm} \tag{19}$$

Accounting for roller chamfers and end crowning, the effective contact length is specified as:

$$l_{\mathrm{eff}} = 90\ \mathrm{mm} \tag{20}$$

The equivalent elastic modulus for steel-on-steel line contact follows:

$$\frac{1}{E'} = \frac{1-\nu_1^2}{E_1} + \frac{1-\nu_2^2}{E_2} \tag{21}$$

Both contact bodies are bearing steel, with material parameters $E_1 = E_2 = 210\text{GPa}$ and $\nu_1 = \nu_2 = 0.30$. Substitution gives:

$$E' = \frac{E}{2(1-\nu^2)} = \frac{210}{2(1-0.30^2)} = 115.4\text{GPa} \tag{22}$$

The roller-raceway pair is approximated as a cylinder-flat line contact, and the equivalent radius of curvature is taken as:

$$R' \approx R_1 = 44.975 \text{ mm} \tag{23}$$

235 The half-width of the Hertzian contact zone is expressed as:

$$b = \sqrt{\frac{4Q_{\max}R'}{\pi l_{\text{eff}}E'}} \tag{24}$$

The maximum Hertzian contact pressure is defined by:

$$p_0 = \frac{2Q_{\max}}{\pi b l_{eff}} \tag{25}$$

Substitute $Q_{\max} = 109\text{kN}, R' = 44.975 \text{ mm}, l_{\text{eff}} = 90 \text{ mm}$ and $E' = 115.4\text{GPa}$ into Eqs. (24) and (25), which yields:

240

$$b = \left[\frac{4 \times 109 \times 10^3 \times 44.975 \times 10^{-3}}{\pi \times 90 \times 10^{-3} \times 115.4 \times 10^9}\right]^{1/2} = 0.777 \text{ mm} \tag{26}$$

$$p_0 = \frac{2 \times 109 \times 10^3}{\pi \times 0.777 \times 10^{-3} \times 90 \times 10^{-3}} = 0.997\text{GPa} \tag{27}$$

The maximum subsurface orthogonal shear stress and its depth under line contact can be approximated as:

$$\tau_{\max} \approx 0.30 p_0 = 0.30 \times 0.997 = 0.299\text{GPa} \tag{28}$$

$$z_\tau \approx 0.78b = 0.78 \times 0.777 = 0.606 \text{ mm} \tag{29}$$

To examine sensitivity to roller-end loading caused by skew, raceway deformation or mounting-surface misalignment, the nominal Hertz pressure is multiplied by a dimensionless edge-load factor Kedge. The system FEA provides independent
245 structural motivation for this sensitivity analysis: it predicts 0.17° mounting-surface tilt and 0.067° maximum raceway misalignment, while teardown shows roller-end damage and gearbox-side cage contact. Across the 100 mm roller length, 0.067° corresponds geometrically to an end-to-end offset Δg ≈ 100 mm × tan(0.067°) ≈ 0.12 mm. Relative to the nominal Hertz contact half-width b ≈ 0.777 mm at the baseline load, Δg/b ≈ 0.15 (or about 7.7% of the full Hertz contact width 2b). This is not a contact-pressure solution, because the system-level misalignment is redistributed by roller crowning, ring/support
250 compliance, operating clearance and local contact truncation. It does, however, show that the predicted deformation is not negligible relative to the nominal contact scale. The Kedge = 1.20–1.50 sweep is therefore used as an order-of-magnitude, moderate edge-pressure redistribution band (20–50% amplification) that is structurally consistent with a non-negligible skew/misalignment condition, rather than as a purely arbitrary multiplier. Kedge is not back-calculated from 0.067° and remains to be calibrated by roller-resolved thermo-mechanical contact analysis:

255

$$p_{\text{edge}} = K_{\text{edge}}\, p_0 \tag{30}$$

The corresponding local maximum shear stress is:

$$\tau_{\text{edge}} = 0.30 p_{\text{edge}} = 0.30 K_{\text{edge}}\, p_0 \tag{31}$$

The sweep Kedge = 1.00, 1.20, 1.35 and 1.50 represents, by definition, 0%, 20%, 35% and 50% increases in local peak pressure relative to the nominal Hertzian baseline while retaining the same baseline roller load. The upper value is intentionally a bounded 'strong amplification' scenario rather than an asserted field maximum. This range is used to answer the conditional question 'how much would the local stress scale change if plausible end loading amplified the nominal peak by 20–50%?' The calculation therefore supports sensitivity of fatigue-driving stress to edge loading, but it cannot establish that any particular Kedge occurred in service. Roller-resolved thermo-mechanical contact analysis is required to determine a physical amplification factor.

$$p_{\text{edge}} = 1.20 - 1.50\text{GPa}, \tau_{\text{edge}} = 0.36 - 0.45\text{GPa} \tag{32}$$

3.4 Indicative elastohydrodynamic film-ratio sensitivity

A simplified Hamrock–Dowson-type minimum-film-thickness expression is used only as an indicative elastohydrodynamic sensitivity screen (Hamrock and Dowson, 1981). The classical formulation is fundamentally a steady, fully supplied, Newtonian oil-film solution for idealized smooth elastic contacts; applying it to a very large, slow, grease-lubricated wind-turbine main bearing introduces several important mismatches. First, grease lubrication is replenishment-limited: the rolling track may experience starvation, channeling and intermittent reflow, whereas the fully flooded solution assumes lubricant is continuously available at the inlet. Second, grease rheology is not represented by a single base-oil viscosity: thickener structure, shear history, bleed, degradation and temperature-dependent non-Newtonian behavior can change inlet supply and effective traction. Third, the turbine operates under variable speed, load, reversal/oscillation and transient thermal conditions, while the analytical expression is quasi-steady. Fourth, roller skew, end effects, surface distress, debris and local roughness evolution violate the ideal line-contact and uniform-surface assumptions. Hart et al. (2022a) explicitly caution that EHL formulas must be interpreted within their assumptions, and their main-bearing simulations show strong sensitivity to operating and replenishment conditions (Hart et al., 2022b). The roughness values used below (Rq = 0.2, 0.4 and 0.8 micrometres) are illustrative scenarios, not measured roughness values from the failed raceways. Therefore the calculated hmin and Lambda are not estimates of the in-service grease-film thickness or a diagnosis of mixed/boundary lubrication; they provide only a controlled baseline showing how nominal film ratio varies with assumed roughness and specified operating inputs.

$$U = \frac{\eta_0 u}{E' R_x} \tag{33}$$

$$G = \alpha E' \tag{34}$$

$$W = \frac{Q_{\max}}{E' R_x^2} \tag{35}$$

The minimum film thickness is given by:

$$\frac{h_{\min}}{R_x} = 3.63 U^{0.68} G^{0.49} W^{-0.073} \tag{36}$$

Substitute $\eta_0 = 0.16\ \text{Pa} \cdot \text{s}, u = 1.0\ \text{m/s}, \alpha = 2.0 \times 10^{-8}\ \text{Pa}^{-1}, R_x = 44.975\ \text{mm}$ into Eqs. (33)-(35):

https://doi.org/10.5194/wes-2026-144
Preprint. Discussion started: 10 September 2026

$$U = \frac{0.16 \times 1.0}{115.4 \times 10^9 \times 44.975 \times 10^{-3}} = 3.08 \times 10^{-11} \tag{37}$$

$$G = 2.0 \times 10^{-8} \times 115.4 \times 10^9 = 2.31 \times 10^3 \tag{38}$$

$$W = \frac{109 \times 10^3}{115.4 \times 10^9 \times (44.975 \times 10^{-3})^2} = 4.69 \times 10^{-4} \tag{39}$$

From Eq. (36):

$$h_{\min} = 0.90\mu \text{ m} \tag{40}$$

The film thickness ratio is defined as:

$$\Lambda = \frac{h_{\min}}{\sqrt{R_{q1}^2 + R_{q2}^2}} \tag{41}$$

If the surface roughness of the roller and raceway is identical, i.e. $R_{q1} = R_{q2} = R_q$, the expression simplifies to:

$$\Lambda = \frac{h_{\min}}{\sqrt{2}R_q} \tag{42}$$

Substitute $h_{\min} = 0.90\mu$ m, and we obtain Table 3 data.

Table 3: Idealized film-ratio sensitivity to assumed surface roughness.

Rq	**Λ**	Conventional Lambda interpretation (idealized)
0.2 μm	3.20	Near full-film lubrication
0.4 μm	1.60	Mixed lubrication
0.8 μm	0.80	Boundary lubrication

Under the idealized fully supplied assumptions, the calculated film ratio spans near full-film to boundary-like values as roughness is varied. The result should be read as a reference sensitivity map: it identifies how close an idealized contact could move toward low-Lambda conditions if the effective roughness increases, but it does not quantify starvation or grease replenishment. In the actual bearing, restricted inlet access, transient low-speed operation, debris, surface damage and grease rheology could make the true inlet condition either poorer or temporally more variable than the fully supplied baseline. Because none of those effects is solved here, the manuscript uses the film-ratio calculation only to support the plausibility of reduced film robustness and never as direct evidence that the failed contacts operated at a particular lubrication regime (Hart et al., 2022a, b).

3.5 Load sensitivity and descriptive case-depth-to-shear-depth ratio

Since the ultimate loads from on-site Bladed simulations, load cases for unit selection calculations, and engineering reference loads are not fully consistent, this paper adopts an identical roller load distribution model to conduct a sensitivity analysis with respect to radial load. Combining Equations (17), (24), (25) and (29), the following expressions are derived:

https://doi.org/10.5194/wes-2026-144
Preprint. Discussion started: 10 September 2026

$$Q_{\max}(F_r) = \frac{F_r}{\sum_{j=1}^{Z_r}\left[1 - \frac{1}{2\varepsilon}\left(1-\cos\psi_j\right)\right]^t \cos\psi_j} \tag{43}$$

$$b(F_r) = \left(\frac{4Q_{\max}(F_r)R'}{\pi l_{\mathrm{eff}} E'}\right)^{\frac{1}{2}} \tag{44}$$

$$p_0(F_r) = \frac{2Q_{\max}(F_r)}{\pi b(F_r) l_{\mathrm{eff}}} \tag{45}$$

$$z_\tau(F_r) = 0.78b(F_r) \tag{46}$$

With fixed parameters Zr = 72, epsilon = 0.25, an idealized 4–8 o'clock core load zone and t = 10/9, radial-load sensitivity is evaluated using the same discrete Eq. (17) summation for every load level. The 4–8 o'clock sector is not a redefinition of the observed 3–9 o'clock damage envelope. At 5° roller pitch, the -60° to +60° discretization contains 25 roller-centre positions, with the two boundary positions carrying zero load and 23 positions carrying positive load under the idealized distribution. Here, Fr = 1.9346 MN is the maximum radial resultant Fyz,max from the LM73.5 rotating hub-centre design-extreme dataset; Fr = 2.266 MN is the equivalent radial load in the bearing-selection calculation. These design values are used for sensitivity scaling, not as synchronized failure-event loads. Sensitivity to a wider or narrower load-support angle should be addressed in a future roller-resolved internal-load model rather than inferred from the circumferential extent of spalling.

It can be observed that as the radial load increases from 1.20 MN to 2.266 MN , the nominal contact pressure rises from 0.891 GPa to 1.225 GPa , and the depth of maximum shear stress increases from 0.542 mm to 0.745 mm . The maximum radial resultant force of the bladed case corresponds to $Q_{\max} = 141.2\mathrm{kN}, p_0 = 1.132\mathrm{GPa}$ and $z_\tau = 0.688$ mm, which are higher than the baseline working condition in this paper.

The contact pressure and shear stress under edge loading are given by Eqs. (30) and (31):

$$p_{\mathrm{edge}}\left(K_{\mathrm{edge}}\right) = K_{\mathrm{edge}}\, p_0 \tag{47}$$

$$\tau_{\mathrm{edge}}\left(K_{\mathrm{edge}}\right) = 0.30 K_{\mathrm{edge}}\, p_0 \tag{48}$$

For the baseline working condition with $p_0 = 0.997\mathrm{GPa}$, we obtain:

For descriptive comparison only, a case-depth-to-shear-depth ratio is defined as the measured effective hardened-layer depth divided by the nominal Hertzian maximum-shear depth:

$$\chi_{\mathrm{SHD}} = \frac{\mathrm{SHD}}{z_\tau} \tag{49}$$

where SHD denotes the measured effective hardened-layer depth and z_tau is the nominal maximum-shear depth from Eq. (46). This ratio is not a standardized design criterion, contains no validated pass/fail threshold and does not account for residual stress, material cleanliness, hardness gradients, local traction or the actual three-dimensional stress field. It is used only to compare the depth scale of selected material observations with the analytical stress-depth scale. Taking the baseline screening condition as an example:$z_\tau z_\tau = 0.606$ mm

The selected OR_A loaded-zone radial samples show a small remaining depth ratio, while the unworn OR_B radial sections have a lower effective case depth than the selected axial sections. Because OR_A samples were already worn or spalled, the ratio cannot reconstruct their as-manufactured condition. For OR_B, the comparison indicates circumferential/row variability in measured case depth but, without drawing acceptance limits, residual-stress data and broader unworn mapping, it cannot establish a manufacturing nonconformity or predict fatigue life.

3.6 Local roller–raceway contact-pressure map

To relate turbine-level loading to the local roller–raceway stress scale, a semi-analytical contact-pressure map is constructed from the Bladed radial-load case, Hertzian line-contact solution and an assumed edge-load amplification function. The map is explicitly a parametric visualization: neither the edge-load factor nor the axial pressure shape is calibrated against roller-resolved measurements. The model therefore illustrates stress localization that would be expected if skew-induced amplification occurs; it does not reconstruct the actual field pressure distribution. Its primary purpose is to define transparent sensitivity cases and boundary conditions for future three-dimensional thermo-mechanical contact analysis.

Combining field failure evidence with contact mechanics and finite-element analysis is widely used to investigate rolling contact fatigue and wind-turbine bearing failures (Lee et al., 2025; Ren et al., 2025; Chen et al., 2024; Kawiak and Sajek, 2025; Yin et al., 2024; Ishihara et al., 2025; Wang et al., 2022).

The local contact pressure is expressed as:

$$p(x,y) = p_0\sqrt{1-(y/b)^2}\, f_{\mathrm{edge}}(x), \quad |y| \le b \tag{50}$$

$$p(x,y) = 0, \quad |y| > b \tag{51}$$

where x denotes the roller axial coordinate, y is the coordinate along the contact-width direction, b is the Hertz contact half-width, and f_edge(x) is the axial edge-load amplification function. The roller axial coordinate range used here is:

$$-\frac{L}{2} \le x \le \frac{L}{2} \tag{52}$$

Case 1: No edge load

$$f_{\mathrm{edge}}(x) = 1 \tag{53}$$

Case 2: Linear edge-load function (applicable when roller skew, ring deformation or mounting-surface misalignment occurs)

$$f_{\mathrm{edge}}(x) = \frac{1+(K_{\mathrm{edge}}-1)x/(L/2)}{1+(K_{\mathrm{edge}}-1)|x|/(L/2)}, \quad -\frac{L}{2} \le x \le \frac{L}{2} \tag{54}$$

In Eq. (54), the denominator preserves the axial-average load level, while K_edge controls the end-side pressure amplification. The amplified end-side peak pressure is approximated by:

$$p_{\max} \approx K_{\mathrm{edge}} p_0 \tag{55}$$

https://doi.org/10.5194/wes-2026-144
Preprint. Discussion started: 10 September 2026

Figure 4: Semi-analytical local roller–raceway contact-pressure sensitivity map for the Bladed maximum radial-load case (Fr = 1.9346 MN) with Kedge = 1.35. Pressure is shown in GPa; the map is a parametric sensitivity result, not a reconstructed field pressure distribution.

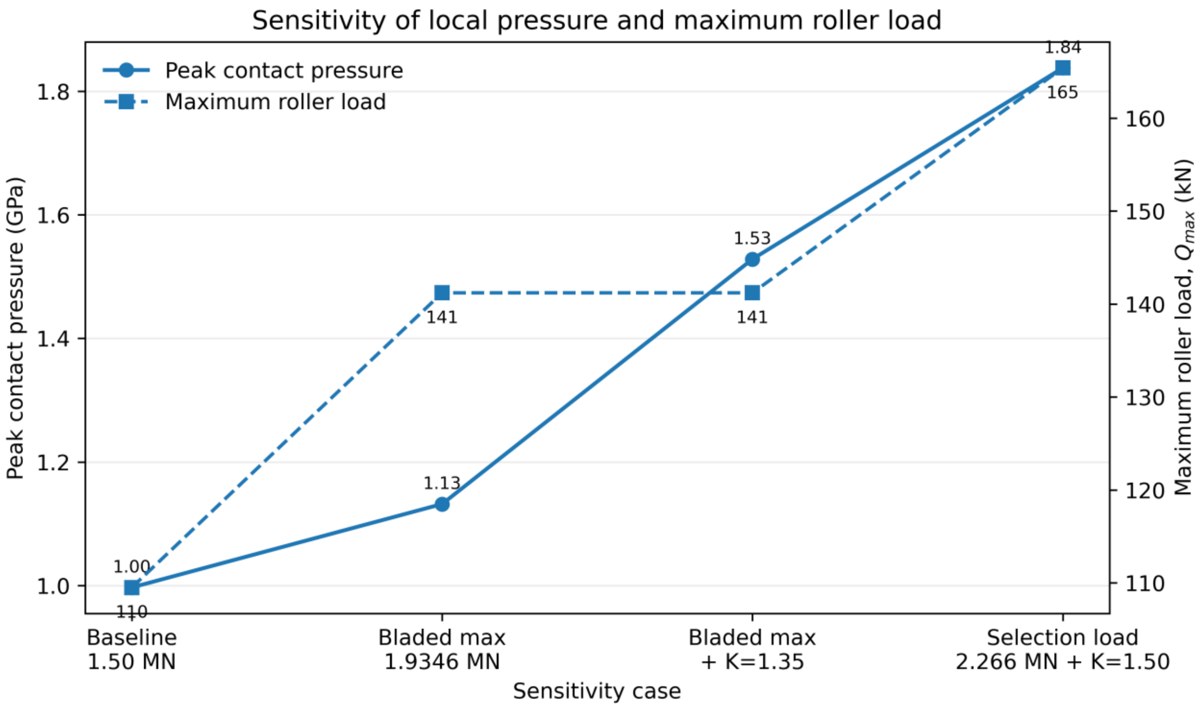

Figure 5: Sensitivity of peak contact pressure (GPa) and maximum single-roller load Qmax (kN) across the four analytical load/edge-amplification cases.

4 Results and mechanism interpretation

4.1 Failure location: continuous belt-like spalling in the radial load zone

All eight dismantled bearings showed damage within the stationary lower radial load zone between 3 and 9 o'clock, whereas axial-row damage was comparatively limited. This repeated spatial pattern identifies local radial load-zone contact as the primary location-controlling condition; it does not by itself identify the initiating material or lubrication mechanism.

4.2 Crack initiation: Hertzian stress and edge loading

Nominal Hertz pressure is a Class-I screening result rather than a measured field maximum. The Class-D evidence consists of roller-end damage, gearbox-side cage contact, and system-level deformation outputs including 0.17° mounting-face tilt and 0.067° raceway misalignment. The 0.067° misalignment corresponds to an approximately 0.12 mm end-to-end geometric offset over the 100 mm roller length, about 15% of the nominal Hertz half-width at the baseline load. This scale comparison makes a moderate edge-pressure redistribution physically plausible, but it does not uniquely map misalignment to pressure amplification because crown geometry, ring flexibility, hot clearance and local support stiffness are not resolved. The Kedge

https://doi.org/10.5194/wes-2026-144
Preprint. Discussion started: 10 September 2026

= 1.20–1.50 sweep therefore asks a bounded conditional question: if this non-negligible geometric misalignment produces a 20–50% local peak-pressure amplification, how would the local pressure and shear-stress scales respond? The resulting 1.20–1.50 GPa values are sensitivity outcomes, not reconstructed field stresses. The Class-H statement remains limited to: thermo-structural deformation may produce roller-end load concentration sufficient to accelerate local RCF. A coupled roller-resolved model using measured hot clearance, actual crowning and support deformation is required to calibrate Kedge quantitatively.

4.3 Crack propagation: mixed lubrication and abrasive contamination

The idealized film-ratio sensitivity shows that roughness changes can move the calculated contact from near full-film toward mixed or boundary-like values. Elevated Fe and Cu are consistent with steel roller/raceway wear and copper cage wear, while teardown showed gearbox-side cage displacement capable of partly obscuring radial-row inlets and non-uniform outlet behavior. Together these observations support a restricted-replenishment pathway, but they do not measure contact-inlet flow or in-service film thickness. The lubrication calculation is therefore used to demonstrate sensitivity, not to assign a field lubrication regime (Hart et al., 2022a, b).

4.4 Material condition as a potential fatigue-margin modifier

Selected OR_A loaded-zone samples showed low residual hardness or little measurable remaining case, while unworn OR_B radial sections had lower effective case depth than the selected axial sections. This is consistent with a possible reduction in local material fatigue margin, but worn samples cannot establish their as-manufactured condition and the row-to-row comparison is not a manufacturing acceptance test. The SHD/z_tau quantity is therefore retained only as a descriptive depth-scale ratio; it is neither a standardized criterion nor a fatigue-life predictor.

4.5 Evidence stratification for WEC and WEA

WEC/WEA is often discussed in wind-turbine bearing premature failure [Lopez-Urunuela et al., 2021; Spille et al., 2021; Mayweg et al., 2021]. In this study, evidence is stratified. The OR_A and OR_B material reports did not explicitly identify WEC or WEA. However, another same-type severe failure sample showed WEC near radial-raceway wear grooves, subsurface cracks and spalling pits. WEC/WEA is therefore not excluded; it is treated as an important accompanying crack-growth mechanism in some severe samples, more likely promoted by high load, edge loading, mixed lubrication and insufficient material fatigue margin than acting as a single initial root cause [Lee et al., 2025; Lopez-Urunuela et al., 2021; Spille et al., 2021; Mayweg et al., 2021].

Table 4: Mechanism evidence matrix and recommended additional validation.

Mechanism	Available evidence	Judgement in this paper
Conventional RCF	Damage in the fixed 3-9 o'clock radial load zone; Hertz/shear-depth consistency	Class D + I: dominant damage mode and location control; initiation mechanism not uniquely identified

Mechanism	Available evidence	Judgement in this paper
Restricted replenishment / abrasive wear	Cage-inlet interference, outlet imbalance, Fe/Cu screens and severe-sample debris	Class D supports restricted-path concern; Class H for contact-level starvation because inlet flow is unmeasured
Edge loading / load redistribution	Roller-end damage, support tilt/misalignment, thermal-clearance pathway	Class D deformation/end-damage evidence + Class I sensitivity; Class H for actual roller-end field stress
Case-condition variability	Low remaining OR_A loaded-zone condition; OR_B radial SHD below axial SHD	Class D material variability; potential fatigue-margin modifier, but original manufacturing state not reconstructed
WEC/WEA	Absent from OR_A/OR_B reports; present in one same-type severe third-party sample	Class D in one same-type severe sample only; possible accompanying crack-growth feature, not a universal initiator

4.6 Proposed crack-initiation and propagation pathway

The working hypothesis is: repeated fixed radial load-zone contact produces cyclic subsurface and near-surface stress; thermo-structural clearance change and support deformation can modify roller load sharing; if roller-end loading occurs, local pressure increases; if effective grease delivery is restricted, roughness and debris reduce film robustness; cracks may then initiate at or near the surface or subsurface, propagate by rolling contact fatigue, and coalesce into block and belt-like spalling. The sequence contains conditional links ('can'/'if') because hot clearance, inlet flow and crack origin were not measured synchronously. WEC/WEA may accompany crack growth in some samples but is not required to explain the common fleet morphology.

4.7 Evidence chain and testable predictions

The evidence chain is summarized as:

https://doi.org/10.5194/wes-2026-144
Preprint. Discussion started: 10 September 2026

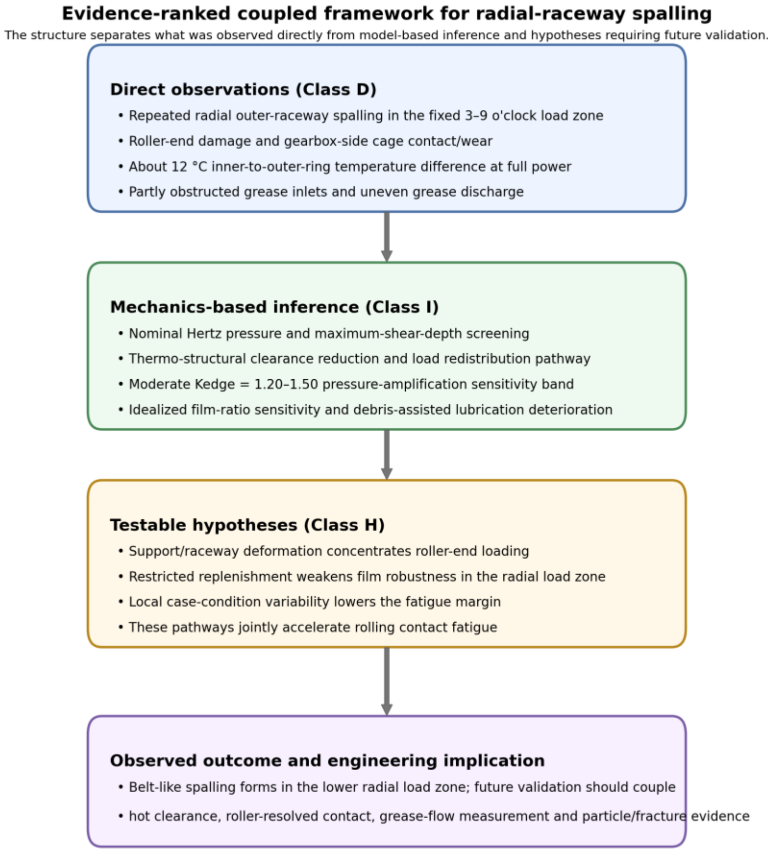

Figure 6: Evidence-ranked coupled framework for belt-like radial-raceway spalling, with balanced box proportions and a clearer separation of direct observations, mechanics-based inference and testable hypotheses.

The framework predicts that severe units should show spatial agreement between damage and the fixed lower load zone, more frequent roller-end/cage contact, reduced hot operating clearance or uneven load sharing, lower effective grease flow at selected radial inlets, Fe/Cu particles with diagnostic morphology, and lower local fatigue margin where case condition is abnormal. These predictions define prospective validation tests rather than conclusions assumed from the current data.

5 Discussion and engineering implications

5.1 Coupled mechanism rather than a single-factor explanation

No single measured factor explains the fleet pattern. Using the evidence hierarchy, the strongest Class-D evidence is spatial: all dismantled bearings failed within the stationary lower radial load zone while axial rows were comparatively less affected. Additional Class-D observations include roller-end damage, cage displacement/inlet interference, non-uniform outlet behavior, the available ring-temperature difference and material-test results. Class-I calculations show that contact stress is sensitive to

https://doi.org/10.5194/wes-2026-144
Preprint. Discussion started: 10 September 2026

radial load and assumed edge amplification, and that idealized film ratio is sensitive to roughness and operating inputs; these calculations establish mechanical plausibility, not field calibration. Class-H statements connect those observations into a falsifiable coupled mechanism: thermo-structural clearance/deformation may redistribute roller load, restricted grease replenishment may weaken film robustness, and local case-condition variability may reduce fatigue tolerance. The resulting interpretation is therefore a ranked coupled hypothesis, not a decomposition of causal contribution percentages and not proof that every proposed pathway operated simultaneously in every failed bearing.

5.2 Difference between standard rating life and fleet observations

The combined and radial modified reference lives are 220901 h and 295536 h, respectively, whereas the removed bearings had 26–53 calendar months of service. Calendar service and rating-life operating hours are not directly equivalent because rotor operating hours and load spectra for each removed unit were not reconstructed. Even an upper-bound assumption of continuous operation for 53 months corresponds to only about 38.7 kh, still well below the calculated reference lives; however, this comparison is used only to demonstrate the scale of the field-life gap and not to estimate a life-consumption ratio or validate a probabilistic failure model. The discrepancy does not invalidate ISO rating methods. Rather, it motivates examination of design-stage simplifications in local load distribution, support elasticity, operating clearance and lubrication. Recent WES work likewise shows that rating life is sensitive to wind-farm loading and model fidelity (Menck et al., 2025; Quick et al., 2026; Kenworthy et al., 2024; Hart et al., 2020).

5.3 Distinction from false brinelling and a yaw-moment-only explanation

Parked-state vibration or low-speed oscillation can produce false-brinelling/fretting marks and may contribute to surface distress, but it does not alone explain the continuous deep belt-like spalling, severe roller-edge breakage and recurring 3-9 o'clock load-zone distribution. Likewise, Mz is one bending/yaw-related component in the selected hub coordinate system; the Bladed data show that radial resultant Fyz and bending resultant Myz peak in different load cases. The evidence therefore supports combined radial load, bending, clearance, support deformation and tribological effects rather than a single yaw-moment cause.

5.4 Engineering implications: design validation and fleet risk stratification

Design and validation priorities for subsequent bearing generations are:

1. Lubrication path: verify contact-inlet flow on both sides of the radial row; prevent cage displacement from obscuring ports; quantify outlet imbalance; and validate replenishment under cold, hot, parked and low-speed oscillatory conditions.
2. Case condition: define effective case-depth and hardness requirements from contact stress, residual stress and drawing acceptance limits; inspect unworn multi-circumferential sections rather than inferring original quality from a worn loaded-zone section.
3. Contact geometry: validate roller crowning, ring support deformation, mounting-surface tilt and hot operating clearance in a coupled three-dimensional contact model before setting an edge-load-factor limit.

Fleet screening of 203 in-service turbines

The project Cu and Fe results are reported in ppm and are used as internal screening variables together with trend, particle morphology, temperature, vibration and endoscopic evidence. The 198-unit screen is not a survival or prognostic dataset, and

https://doi.org/10.5194/wes-2026-144
Preprint. Discussion started: 10 September 2026

grease age, sampling position and sampling interval were not harmonized across all samples. The numerical thresholds below therefore reproduce project-defined screening logic and must not be interpreted as universal diagnostic limits or transferable failure thresholds:

- · Routine tier: no elevated project grease flag and stable trends; continue periodic grease, temperature and vibration monitoring.
- · Elevated tier: Cu ≥ 5000 ppm or Fe ≥ 5000 ppm, or a rising within-unit trend; shorten the sampling interval and add particle morphology plus targeted inspection.
- · Priority tier: Cu > 10000 ppm together with Fe > 5000 ppm (five of 198 screened units); perform engineering review and condition-based intervention. This category identifies priority for investigation, not automatic proof of bearing failure or a predetermined replacement decision.

The operational value of the three-tier screen is logistical rather than prognostic: it is intended to align inspection urgency with offshore access windows, not to predict remaining life from Cu or Fe. Routine units remain under scheduled monitoring; elevated units are brought forward for repeat sampling and targeted inspection; priority units trigger engineering review early enough to coordinate vessel, crane, spares and weather-window planning. Offshore experience shows that reactive major-component maintenance can involve prolonged shutdowns and high vessel/logistics exposure (Wada et al., 2026), although those external cases are not cost estimates for the present fixed-bottom fleet. For the 5 MW turbine studied here, one unavailable day has a theoretical upper-bound energy exposure of 120 MWh at rated output; actual lost production and any LCOE benefit must be calculated with site-specific wind, availability, curtailment, electricity-value and maintenance-cost data. The engineering value of the tiered framework is therefore the potential to shift decisions from unscheduled failure response toward evidence-triggered inspection and planned heavy maintenance, without claiming a quantified project-specific cost saving.

5.5 Limitations and prospective validation

This retrospective study has six main limitations:

(1) Contact calculations are analytical or system-level; full thermo-mechanical three-dimensional roller-raceway contact stress, including measured hot clearance, has not been solved.

(2) Contact-inlet grease flow, film thickness and particle morphology were not measured synchronously across the fleet. Cu and Fe concentrations are available in ppm, but grease age, sampling position, sampling interval and laboratory/reporting conditions were not fully harmonized across the retrospective records. Therefore, the project thresholds are retained only for internal screening and cannot be assumed to be transferable diagnostic concentration limits.

(3) Loaded-zone material samples were worn or spalled and intact same-model circumferential baselines are incomplete. Prospective work should add cold/hot clearance, instrumented inlet/outlet flow, unworn hardness/case-depth maps, residual stress, spall cross-section SEM/EDS and fracture-origin analysis.

(4) The fleet dataset is not a survival-analysis cohort. The 8/203 removed fraction, 10/203 affected fraction and grease-screening proportions are descriptive cumulative fractions at the 11 August 2026 cut-off. Turbine-specific commissioning dates, observation times, right-censoring, competing interventions and the removal-selection process were not harmonized;

consequently, Kaplan–Meier survival, cumulative incidence, hazard rate and exposure-normalized failure rate are not estimated. A future fleet study should reconstruct unit-level time origin, censoring and covariates before making probabilistic reliability claims.

(5) The available full-power ring-temperature difference is a pathway observation rather than a fleet-wide thermal distribution. Without synchronized multi-location temperature and clearance measurements, it cannot be used to calculate the magnitude or frequency of hot-clearance reduction.

(6) The Bladed and system-FEA datasets are engineering design/extreme-load analyses rather than synchronized time histories from the failed turbines, and the dismantled/material-test samples form a failure-selected case series rather than a randomized case-control design. They therefore support mechanical plausibility and failure morphology, but not event-specific load reconstruction, population-level risk ratios or causal effect sizes.

6 Conclusions

1. In the 203-turbine offshore 5/6.2 MW fleet, eight three-row main bearings had been removed and two units were stopped awaiting replacement by 11 August 2026. The removed bearings had 26–53 calendar months of service (median 48 months). These calendar durations are descriptive and are not treated as operating-hour survival data.
2. All eight dismantled bearings showed damage within the stationary lower radial load zone between 3 and 9 o'clock, whereas axial-row damage was comparatively limited. This repeated spatial pattern identifies local radial load-zone contact as the primary location-controlling condition; it does not by itself identify the initiating material or lubrication mechanism.
3. Under the stated analytical assumptions, direct discrete evaluation of the Stribeck equilibrium in Eq. (17) gives a denominator of 13.700 and a nominal maximum single-roller load of 109.5 kN for Fr = 1.50 MN, without an empirical load-distribution multiplier. The corresponding baseline Hertz pressure is 0.997 GPa and the nominal maximum-shear depth is 0.606 mm. The 4–8 o'clock analytical sector represents a 120° core load-support zone nested inside, but not fitted to, the observed 3–9 o'clock damage envelope. The available system FEA predicts 0.17° mounting-face tilt and 0.067° maximum raceway misalignment; across a 100 mm roller length the latter corresponds to an approximately 0.12 mm end-to-end geometric offset, about 15% of the nominal Hertz half-width. This scale comparison supports a bounded Kedge sensitivity sweep but does not calibrate the factor or reconstruct the field peak stress.
4. In the available full-power observation, the inner ring was about 12 °C hotter than the outer ring at 6 o'clock. Together with 0.45–0.55 mm manufactured radial clearance and system flexibility, this is consistent with a possible clearance-reduction and load-redistribution pathway, but it is not a fleet-wide thermal characterization or stand-alone proof of overload.
5. Recorded top-up does not exclude restricted effective grease delivery. Cage displacement, inlet interference and outlet imbalance are direct observations that motivate a replenishment hypothesis. The Hamrock–Dowson calculation is only a

https://doi.org/10.5194/wes-2026-144
Preprint. Discussion started: 10 September 2026

fully supplied EHL baseline and does not model grease starvation, thickener rheology, transient replenishment, reversal/oscillation or debris; it therefore cannot identify the in-service lubrication regime. The ppm-based Cu/Fe screening values support prioritization only and, because the 198-unit dataset is not a harmonized time-to-event cohort, they are not used as quantitative predictors of bearing failure.

6. Selected material results show non-uniform remaining radial case condition, but worn loaded-zone sections cannot by themselves prove original manufacturing nonconformity; unworn circumferential mapping and drawing acceptance limits are required.
7. The most defensible interpretation is a testable coupled rolling-contact-fatigue hypothesis constructed from explicitly separated evidence levels. Direct observations establish the repeatable lower-load-zone morphology and document roller-end/cage contact, temperature, lubrication-path geometry, material condition and fleet counts. Mechanics-based inferences show that the documented loads and deformations are compatible with stress redistribution and that the idealized film ratio is sensitive to surface/operating conditions, but they do not measure hot clearance, edge pressure or grease-film thickness. The hypotheses are that thermo-structural deformation can concentrate roller load, restricted replenishment can reduce film robustness, and local case-condition variability can lower fatigue tolerance; these links remain falsifiable because synchronized measurements of flow, temperature, hot clearance, roller-resolved contact and fracture origin could confirm or reject them. The study therefore explains the recurrent spatial pattern without claiming a unique initiating event or quantified causal share for each pathway.

Code and data availability

The underlying evidence includes anonymized bearing rating calculations, system finite-element reports, failed-part material tests, disassembly observations, Bladed load reports, temperature observations, grease-screening statistics, and calculation scripts. Project- and supplier-identifying materials cannot be made publicly available because of commercial confidentiality obligations. Anonymized data and calculation scripts may be made available by the corresponding author upon reasonable request, subject to the applicable confidentiality constraints. Detailed rating, FEA, Bladed-load and sensitivity tables that are not essential to the narrative are provided in the Supplement.

Author contributions

XM: Conceptualization, Data curation, Formal analysis, Investigation, Methodology, Software, Visualization, and Writing – original draft. DJ: Conceptualization, Methodology, Project administration, Resources, Supervision, Validation, and Writing – review & editing. KZ: Investigation, Resources, Validation, and Writing – review & editing.

Competing interests

Xilei Ma and Kai Zhang are employed by CSSC Science & Technology Co., Ltd. The field data used in this study originate from internal engineering projects of the company. The authors declare that the research was conducted independently of commercial interests, and no commercial funding was received specifically for this publication. All conclusions and interpretations are presented by the authors on the basis of the evidence described in the manuscript. No other competing interests are declared.

Acknowledgements

The authors acknowledge the field disassembly, condition-monitoring, materials-testing and engineering teams that provided failure photographs, inspection reports and calculation evidence. Project names and turbine identifiers are anonymized. OpenAI ChatGPT was used for English-language editing and manuscript-formatting assistance. The authors remain responsible for the scientific content, calculations, interpretation, and verification of all sources. Figures 1–3 were prepared from author-supplied project photographs and were recomposed to remove internal report overlays and project-identifying labels; the scientific image content was not otherwise altered.

Financial support

This research received no external financial support.

Appendix A

Table A1: Fleet exposure and thresholded grease-screening summary at 11 August 2026

Metric	Count / value	Proportion	Interpretation
Fleet population	203	100%	Exposure denominator
Removed bearings	8	3.94%	Dismantled evidence
Stopped / awaiting replacement	2	0.99%	Additional affected units
Grease-screened units	198	97.54% of fleet	Screening denominator
Cu ≥ 5000 ppm	21	10.61% of screened	Elevated screening flag
Cu > 10000 ppm	14	7.07% of screened	High-Cu flag
Fe ≥ 5000 ppm	10	5.05% of screened	Elevated screening flag
Fe > 10000 ppm	3	1.52% of screened	High-Fe flag

https://doi.org/10.5194/wes-2026-144
Preprint. Discussion started: 10 September 2026

WIND ENERGY SCIENCE DISCUSSIONS

Metric	Count / value	Proportion	Interpretation
Cu > 10000 ppm and Fe > 5000 ppm	5	2.53% of screened	Priority combined flag
Removed-bearing service duration	26-53 months	Median 48 months	Below modified reference life
Evidence boundary	Project screening thresholds	Concentrations reported in ppm	Risk ranking only; not universal diagnostic cut-offs

Table A2: Hardness and effective case depth of selected outer-ring specimens

Sample	Location	Surface or near-surface hardness	Effective case depth
OR_A_1	Axial raceway	59.7-60.1 HRC	5.78 mm
OR_A_1	Radial raceway	27.2-27.7 HRC; 623 HV1 at 0.1 mm	1.49 mm
OR_A_3	Axial raceway	58.5-59.6 HRC	6.13 mm
OR_A_3	Radial raceway	about 275-295 HV1 at 0.1-0.5 mm	No effective case or case essentially lost
OR_B_1	Axial raceway	56.7-56.9 HRC	6.29 mm
OR_B_1	Radial raceway	57.4-58.0 HRC	5.03 mm
OR_B_2	Axial raceway	56.8-57.3 HRC	6.26 mm
OR_B_2	Radial raceway	57.6-57.9 HRC	4.87 mm
OR_B_3	Axial raceway	56.6-57.5 HRC	6.07 mm
OR_B_3	Radial raceway	57.4-57.8 HRC	4.93 mm

References

Chen, D., Zhong, M., Mou, M., Xiao, Q., and Shi, X.: Research on the damage mechanism of the rolling contact fatigue of a wheel–rail contact system under the influences of surface defects, Eng. Fail. Anal., 164, 108631, https://doi.org/10.1016/j.engfailanal.2024.108631, 2024.

Hamrock, B. J. and Dowson, D.: Ball Bearing Lubrication: The Elastohydrodynamics of Elliptical Contacts, Wiley, New York, USA, 1981.

Harris, T. A. and Kotzalas, M. N.: Rolling Bearing Analysis: Essential Concepts of Bearing Technology, 5th edn., CRC Press, Boca Raton, USA, 2006.

Hart, E., Clarke, B., Nicholas, G., Kazemi Amiri, A., Stirling, J., Carroll, J., Dwyer-Joyce, R., McDonald, A., and Long, H.: A review of wind turbine main bearings: Design, operation, modelling, damage mechanisms and fault detection, Wind Energ. Sci., 5, 105–124, https://doi.org/10.5194/wes-5-105-2020, 2020.

Hart, E., de Mello, E., and Dwyer-Joyce, R.: Wind turbine main-bearing lubrication – Part 1: An introductory review of elastohydrodynamic lubrication theory, Wind Energ. Sci., 7, 1021–1042, https://doi.org/10.5194/wes-7-1021-2022, 2022a.

Hart, E., de Mello, E., and Dwyer-Joyce, R.: Wind turbine main-bearing lubrication – Part 2: Simulation-based results for a double-row spherical roller main bearing in a 1.5 MW wind turbine, Wind Energ. Sci., 7, 1533–1550, https://doi.org/10.5194/wes-7-1533-2022, 2022b.

International Electrotechnical Commission: Wind energy generation systems – Part 1: Design requirements, IEC 61400-1:2019, Geneva, Switzerland, 2019.

International Organization for Standardization: Rolling bearings – Dynamic load ratings and rating life, ISO 281:2007, Geneva, Switzerland, 2007.

International Organization for Standardization: Rolling bearings – Methods for calculating the modified reference rating life for universally loaded bearings, ISO/TS 16281:2008, Geneva, Switzerland, 2008.

Ishihara, T., Wang, S., and Kikuchi, Y.: Fatigue prediction of wind turbine main bearing based on field measurement and three-dimensional elastic drivetrain model, Eng. Fail. Anal., 167, 108985, https://doi.org/10.1016/j.engfailanal.2024.108985, 2025.

Jiang, Z., Huang, X., Wang, B., Liao, X., Liu, H., and Ding, P.: Time-dependent reliability-based design optimization of main shaft bearings in wind turbines involving mixed-integer variables, Reliab. Eng. Syst. Saf., 243, 109817, https://doi.org/10.1016/j.ress.2023.109817, 2024.

Johnson, K. L.: Contact Mechanics, Cambridge University Press, Cambridge, UK, 1985.

Kawiak, M. and Sajek, A.: Failure of the roller mill caused by rolling contact, shrinkage stress, and intentionally introduced defects, Eng. Fail. Anal., 179, 109792, https://doi.org/10.1016/j.engfailanal.2025.109792, 2025.

Kenworthy, J., Hart, E., Stirling, J., Stock, A., Keller, J., Guo, Y., Brasseur, J., and Evans, R.: Wind turbine main bearing rating lives as determined by IEC 61400-1 and ISO 281: A critical review and exploratory case study, Wind Energy, 27, 179–197, https://doi.org/10.1002/we.2883, 2024.

Kestel, K., Chesterman, X., Zappalá, D., Watson, S., Li, M., Hart, E., Carroll, J., Vidal, Y., Nejad, A. R., Sheng, S., Guo, Y., Stammler, M., Wirsing, F., Saleh, A., Gregarek, N., Baszenski, T., Decker, T., Knops, M., Jacobs, G., Lehmann, B., König, F., Pereira, I., Daems, P.-J., Peeters, C., and Helsen, J.: Condition monitoring of wind turbine drivetrains: state-of-the-art technologies, recent trends, and future outlook, Wind Energ. Sci., 11, 2103–2155, https://doi.org/10.5194/wes-11-2103-2026, 2026.

Lee, R.-M., Chen, J.-C., and Liu, J.-H.: Advanced analysis of main bearing failure modes and design optimization in MW-sized wind turbines: A multi-physics coupling theoretical framework, Eng. Fail. Anal., 181, 109945, https://doi.org/10.1016/j.engfailanal.2025.109945, 2025.

Lopez-Urunuela, F. J., Fernandez-Diaz, B., Pagano, F., Lopez-Ortega, A., Pinedo, B., Bayon, R., and Aguirrebeitia, J.: Broad review of white etching crack failure in wind turbine gearbox bearings: Main factors and experimental investigations, Int. J. Fatigue, 145, 106091, https://doi.org/10.1016/j.ijfatigue.2020.106091, 2021.

Mayweg, D., Morsdorf, L., Wu, X., and Herbig, M.: The role of carbon in the white etching crack phenomenon in bearing steels, Acta Mater., 203, 116480, https://doi.org/10.1016/j.actamat.2020.11.022, 2021.

Menck, O., Schleich, F., and Stammler, M.: Rolling contact fatigue calculation of a three-row roller pitch bearing in a wind turbine, Wind Energ. Sci., 10, 2771–2789, https://doi.org/10.5194/wes-10-2771-2025, 2025.

Quick, J., Hart, E., Nilsen, M. B., Lund, R. S., Liew, J., Huang, P., Rethore, P.-E., Keller, J., Song, W., and Guo, Y.: Reductions in wind farm main bearing rating lives resulting from wake impingement, Wind Energ. Sci., 11, 493–507, https://doi.org/10.5194/wes-11-493-2026, 2026.

Ren, F., Yang, Z., and Li, Z.: Experimental and numerical investigation into rolling contact fatigue crack initiation on the V-Track test rig, Eng. Fail. Anal., 170, 109206, https://doi.org/10.1016/j.engfailanal.2024.109206, 2025.

Sadeghi, F., Jalalahmadi, B., Slack, T. S., Raje, N., and Arakere, N. K.: A review of rolling contact fatigue, J. Tribol., 131, 041403, https://doi.org/10.1115/1.3209132, 2009.

https://doi.org/10.5194/wes-2026-144
Preprint. Discussion started: 10 September 2026

Spille, J., Wranik, J., Barteldes, S., Mayer, J., Schwedt, A., Zürcher, M., Lutz, T., Wang, L., and Holweger, W.: A study on the initiation processes of white etching cracks (WECs) in AISI 52100 bearing steel, Wear, 477, 203864, https://doi.org/10.1016/j.wear.2021.203864, 2021.

Wada, R., Nejad, A. R., Iijima, K., Shimazaki, J., Ibrion, M., Wanaka, S., Nomura, H., Mizushima, Y., Nakashima, T., and Takagi, K.: Floating offshore wind in Japan: addressing the challenges, efforts, and research gaps for large-scale commercialization, Wind Energ. Sci., 11, 1013–1056, https://doi.org/10.5194/wes-11-1013-2026, 2026.

Wang, S., Du, J., Chen, Y., Wu, S., and Huang, Z.: Influence of elliptical truncation on the raceway in a four-point contact pitching bearing, Eng. Fail. Anal., 141, 106711, https://doi.org/10.1016/j.engfailanal.2022.106711, 2022.

Yin, Y., Shi, P., Zhang, S., Qing, T., Zhou, N., Qian, L., and Chen, L.: Lubrication failure mechanism of rolling-sliding steel ball against oil-impregnated porous polyimide and bearing steel in double friction pair, Eng. Fail. Anal., 164, 108622, https://doi.org/10.1016/j.engfailanal.2024.108622, 2024.